A sub-cell spectral-element simulator for 2D rigid-body-fluid interaction problems

Li-Chieh Chen*, Chien-Ta Lin, Mei-Jiau Huang

Mechanical Engineering Department, National Taiwan University, Taipei, Taiwan 106

ARTICLE INFO

ABSTRACT

In this work, we propose an immersed-boundary-type simulation method for the two-way coupling problems between a rigid body and a fluid. In this simulation tool, the entire fluid-solid domain is treated as an incompressible fluid with non-uniform density and the no-slip boundary condition at the rigid body surface is enforced by the penalization method. The fluid solver is developed in use of the spectral element method for the spatial discretization and the mixed explicit/implicit scheme for the temporal discretization. An additional Lagrangian mesh is employed and attached to the rigid body in order to trace the rigid body and to perform the area integration over the solid domain. Besides, a so-called sub-cell scheme is developed to smooth the discontinuity at the fluid–solid interface. The validity and accuracy of the proposed simulation method were examined well by applying it to the sedimentation problems of circular, triangular, square, as well as elliptic cylinders in a channel. An accuracy of 2nd order was observed, probably due to the use of triangular Lagrangian elements and consequently a piecewise-linear approximation of the rigid body shape and also due to the 2nd-order interpolation involved in the sub-cell scheme.

© 2015 Civil-Comp Ltd. and Elsevier Ltd. All rights reserved.

1. Introduction

The immersed boundary method has become very popular for the FSI (Fluid-Structure Interaction) problems in recent decades mainly because of its great capability in handling complicated fluid–solid interfaces. The immersed boundary method was first proposed by Peskin and his colleagues [1–3] who, when investigating the motion of massless and elastic surfaces in a viscous incompressible fluid, treated the elastic material as part of the fluid and modeled its influence on the fluid motion by a force term. The main advantage of this method is that only one Eulerian mesh is required, together with some Lagrangian markers used to identify the elastic material; body-fitted-meshing thus becomes un-necessary and the method becomes very efficient. This immersed-boundary concept caught a lot of attentions and was employed in successive researches; Various new methods were developed such as the direct forcing method [4], the fictitious domain method [5–12], the immersed finite element method [13–15], and so on.

The direct forcing method was developed by Mohd-Yusof [4] for motion-prescribed structures. A pseudo body force calcultated based on the prescribed motion and the discretized momentum equation was added at the mesh points near the fluid–solid interface in order to fulfill the no-slip boundary condition. To count the two-way coupling effects between the fluid and the rigid bodies, Glowinski et al. [5] proposed the fictitious domain method. In their work, the fluid was extended into the rigid-body region and the fluid momentum equation and the rigid-body motion were linked through a use of Lagrangian multipliers. Instead of employing Lagrangian multipliers, Yu and Shau [6] and Gallier et al. [7] linked the fluid and rigid-body by a pseudo body-force within the rigid-body domain and derived an explicit equation for the pseudo body-force. In the studies of Sharma and Patankar [8] and Apte et al. [9,10], the rigid body was treated as a second fluid with a different density; non-uniform-density fluid momentum equations were then solved. The total momentum of the solution within the solid region was next calculated and taken as the total momentum of the rigid body at the new time step. The non-uniform-density concept was also employed by Coquerelle and Cottet [11] as well as Gazzola et al. [12] when their solving the vorticity equation in use of a vortex method. The penalization method was employed to enforce the rigid body motion. Furthermore, to avoid/reduce the numerical instability arising from the discontinuity, they used a smoothing function to smooth the flow density and the penalization force near the fluid-structure interface. In the immersed finite element methods [13–15], the equations of motion of the strucures were modified into a form similar to that of the fluid momentum equations and differences between them were lumped as the FSI force which was then distributed inside the solid region. Rigid and deformable structures immersed and moving in incompressible

* Corresponding author. Tel: +88 6922506111.
E-mail addresses: b91502126@ntu.edu.tw, mortality19@gmail.com (L.-C. Chen), mjhuang@ntu.edu.tw (M.-J. Huang).

viscous fluid were both attempted and satisfactory results were obtained.

Most of the above methods however adopted low-oder schemes of either the finite element method or the finite volume method for the spatial discreitization. Stationary but complicated structures may also exist in problem and has better be resolved in a traditional way, say by a body-fitted mesh. A high-order scheme can improve further. Such an attempt was ever made by Parussini and Pediroda [16] who implemented the fictitious domain concept with the spectral element method for steady FSI problems. The spectral element method is well known with its high accuracy and high geometric flexibility [17,18]. In the present work, we also prefer the spectral element method but would like to attempt the non-uniform density approach and the penalization method. Besides, we intend to employ a Lagrangian mesh for tracing the solid structure in addition to one Eulerian mesh for the entire computational domain. To overcome the difficulties induced by the discontinuity at the fluid–solid interface, a special approach called "sub-cell scheme" is developed.

It must be mentioned that this work is an extension of a previous work of the authors [19]. The original scheme employed no Lagrangian mesh. It thus could handle only solids which shapes are describable by a mathematic function and a particular piecewise integration method was needed for the solid-region integration. The scheme is now extended to rigid bodies of arbitrary convex shapes with the help of a Lagrangian mesh. The Lagrangian mesh is used not only to trace the rigid body but also to enable the Gaussian quadrature integration over the solid region. Numerical experiments and convergence tests are finished in the present work.

The rest of this paper is arranged as follows: the governing equations are introduced in Section 2; the discretization methods and the proposed sub-cell scheme are described in Section 3; numerical experiments are performed and the validity and the accuracy of the proposed solver are examined in Section 4, and finally conclusion is given in Section 5.

2. Governing equations

In this section, we introduce the physical and the model equations for flow induced by a rigid body immersed and moving in an incompressible Newtonian fluid.

2.1. Physical equations

Let Ω be the physical domain of interest and $\Omega_s(t)$ be the region occupied by the rigid body as shown in Fig. 1; the moving solid boundary is denoted by $\partial\Omega_s(t)$. The governing equations for fluid flow outside the rigid body are the incompressible Navier–Stokes equations:

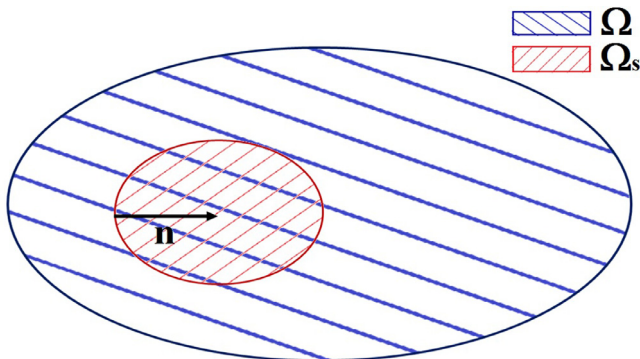$$\nabla \cdot \mathbf{u} = 0, \mathbf{x} \in \Omega/\Omega_s(t) \tag{1}$$

Fig. 1. A solid body Ω_s moving in a physical domain Ω which is full of fluid.

$$\frac{\partial \mathbf{u}}{\partial t} + (\mathbf{u} \cdot \nabla)\mathbf{u} = \frac{1}{\rho_f}\nabla \cdot \sigma + \mathbf{g}, \mathbf{x} \in \Omega/\Omega_s \tag{2}$$

$$\mathbf{u} = \mathbf{u}_s, \mathbf{x} \in \partial\Omega_s(t) \tag{3}$$

where appear the fluid velocity $\mathbf{u}$, the rigid-body velocity $\mathbf{u}_s$, the fluid density ρ_f, and the gravity $\mathbf{g}$. For Newtonian fluids, the stress tensor σ is related to the rate-of-strain tensor $\mathbf{D}$ by

$$\sigma = -p\mathbf{I} + 2\mu_f\mathbf{D}$$

where p is the pressure, μ_f is the fluid dynamic viscosity, and $\mathbf{I}$ is the identity matrix.

On the other hand, the rigid body moves according to the Newton's 2nd law as below:

$$M\frac{d\mathbf{u}_T}{dt} = \mathbf{F} + M\mathbf{g} = -\oint_{\partial\Omega_s} \sigma \cdot \mathbf{n}ds + M\mathbf{g} \tag{4}$$

$$I\frac{d\boldsymbol{\omega}}{dt} = \mathbf{T} = -\oint_{\partial\Omega_s} \sigma \times (\mathbf{x}-\mathbf{x}_c)ds \tag{5}$$

where $\mathbf{F}$ and $\mathbf{T}$ are the instantaneous force and torque exerted by the fluid on the rigid body; M and I are the mass and the moment of inertia, $\mathbf{u}_T$ and $\boldsymbol{\omega}$ are the translational and angular velocities, and $\mathbf{x}_c$ is the mass center of the rigid body respectively; finally $\mathbf{n}$ is the normal unit vector at the interface directing from the fluid into the solid. Finally, the instantaneous velocity at any point $\mathbf{x}$ within the rigid body can be expressed as

$$\mathbf{u}_s(\mathbf{x}, t) = \mathbf{u}_T(t) + \omega(t) \times (\mathbf{x} - \mathbf{x}_c) \tag{6}$$

2.2. Model equations

Following the approach of Coquerelle and Cottet [11], we extend the fluid flow field onto the solid region and add a penalization force ($\mathbf{f}_{pen}$) to enforce the no-slip boundary conditions. The so-built model equations are as follows:

$$\nabla \cdot \mathbf{u} = 0, \mathbf{x} \in \Omega \tag{7}$$

$$\frac{\partial \mathbf{u}}{\partial t} + (\mathbf{u} \cdot \nabla)\mathbf{u} = -\frac{1}{\rho}\nabla p + \nu\nabla^2\mathbf{u} + \mathbf{g} + \mathbf{f}_{pen}, \mathbf{x} \in \Omega \tag{8}$$

$$\rho = \begin{cases} \rho_f, \mathbf{x} \in \Omega/\Omega_s \\ \rho_s, \mathbf{x} \in \Omega_s \end{cases} \tag{9}$$

$$\mathbf{f}_{pen} = \begin{cases} 0, \mathbf{x} \in \Omega/\Omega_s \\ \lambda(\mathbf{u}_s - \mathbf{u}), \mathbf{x} \in \Omega_s \end{cases} \tag{10}$$

where $\nu = \mu_f/\rho_f$, ρ_s is the solid density, and λ is the penalization factor. Equivalently, the solid domain is replaced by an incompressible fluid with a density ρ_s and a kinematic viscosity ν. The penalaztion method has been well studied in the works of Angot et al. [20] and Bost et al. [21]. This method is very easy to implement and the penalty error can be easily controlled by choosing a sufficiently large penalization factor, λ. In practice, the discontinuities in the density field ρ and in the penalty force $\mathbf{f}_{pen}$ often cause numerical instability and must be smoothed away. In the present work, we develop a so-called sub-cell scheme to handle this problem (see Section 3.3).

After Eqs. (7)–(10) are solved for the whole computational domain, the velocity inside the solid region is replaced by $\mathbf{u}_s(\mathbf{x},t)$, namely by Eq. (6), with

$$\mathbf{u}_T = \frac{1}{M}\int_{\Omega_s} \rho\mathbf{u}d\Omega_s \tag{11}$$

and

$$\omega = \frac{1}{I}\int_{\Omega_s} \rho(\mathbf{x} - \mathbf{x}_c) \times \mathbf{u}d\Omega_s \tag{12}$$

3. Numerical scheme

The discretization starts from the time discretization. Herein we chose the 1st order mixed stiffly stable scheme [22]:

$$\frac{\mathbf{u}^{n+1} - \mathbf{u}^n}{\Delta t} = -\frac{1}{\rho}\nabla p^{n+1} - (\mathbf{u}^n \cdot \nabla)\mathbf{u}^n + \nu\nabla^2\mathbf{u}^{n+1}$$
$$+ \lambda\left(\mathbf{u}_s - \mathbf{u}^{n+1}\right) + \mathbf{g} \tag{13}$$

Terms on the right-hand side of Eq. (13) are then counted one by one according to the factional step method [23]. The spatial discretization is executed based on the spectral element method; triangular elements for both Eulerian and Lagrangian meshes were selected. Details are introduced in the following subsections.

3.1. Fractional-step time marching scheme

We split the time marching for each time step (from time t_n to time t_{n+1}) into 4 sub-steps. The nonlinear term and the gravity term in Eq. (13) are dealt first, resulting in an intermediate velocity $\mathbf{u}^*$:

$$\frac{\mathbf{u}^* - \mathbf{u}^n}{\Delta t} = -[(\mathbf{u} \cdot \nabla)\mathbf{u}]^n + \mathbf{g} \tag{14}$$

Next we apply the divergence free condition and solve the following two coupled equations for the pressure p^{n+1} and the velocity $\mathbf{u}^{**}$ by iteration:

$$\frac{\nabla \cdot \rho\mathbf{u}^* - \mathbf{u}^{**} \cdot \nabla\rho}{\Delta t} = \nabla^2 p^{n+1} \tag{15}$$

$$\frac{\mathbf{u}^{**} - \mathbf{u}^*}{\Delta t} = -\frac{1}{\rho}\nabla p^{n+1} \tag{16}$$

The viscous term is dealt implicitly next as follows

$$\frac{\mathbf{u}^{***} - \mathbf{u}^{**}}{\Delta t} = \nu\nabla^2\mathbf{u}^{***} \tag{17}$$

In the present work, Eqs. (15) and (17) are solved by a Helmholtz solver developed based on the Galerkin method and a PCG matrix solver.

We are now ready to update the rigid body motion. The intermediate velocity $\mathbf{u}^{***}$ is first interpolated onto the Gaussian quadrature points of the solid (Lagrangian) elements by using the modal basis functions associated with the Eulerian elements. Solid-region integrations in Eqs. (11) and (12) are then finished by the Gaussian quadrature integration method based on the Lagrangian mesh; consequently

$$\mathbf{u}_T = \frac{1}{M}\int_{\Omega_s}\rho\mathbf{u}^{***}d\Omega_s$$

and

$$\omega = \frac{1}{I}\int_{\Omega_s}\rho(\mathbf{x} - \mathbf{x}_c) \times \mathbf{u}^{***}d\Omega_s \tag{18}$$

The location of the mass center and orientation of the rigid body can be update now by

$$\mathbf{x}_c^{n+1} = \mathbf{x}_c^n + \mathbf{u}_T\Delta t \tag{19}$$

$$\theta^{n+1} = \theta^n + \omega\Delta t \tag{20}$$

To avoid the accumulated distortion due to numerical errors, we update the coordinates of the Lagrangian mesh points in the following way

$$\mathbf{x}_s^{n+1} = \mathbf{x}_c^{n+1} + \begin{bmatrix}\cos\theta^{n+1} - \sin\theta^{n+1} \\ \sin\theta^{n+1} \cos\theta^{n+1}\end{bmatrix}\left(\mathbf{x}_s^0 - \mathbf{x}_c^0\right) \tag{21}$$

where $\mathbf{x}_s^0 - \mathbf{x}_c^0$ is the relative position of the mesh point $\mathbf{x}_s$ to the mass center $\mathbf{x}_c$ at time = 0.

Finally we take care of the penalization term in the following way:

$$\frac{\tilde{\mathbf{u}} - \mathbf{u}^{***}}{\Delta t} = \lambda(\mathbf{u}_s - \tilde{\mathbf{u}}) \tag{22}$$

$$\mathbf{u}^{n+1} = \begin{cases}\mathbf{u}^{***}, \mathbf{x} \in \Omega/\Omega_s \\ \tilde{\mathbf{u}}, \mathbf{x} \in \Omega_s\end{cases} \tag{23}$$

3.2. Modal basis functions

In the spectral element method, an interested physical variable $\psi(x,y)$ is approximated by a linear combination of basis functions ϕ_{pq} with coefficients $\tilde{\psi}_{pq}$ as follows

$$\psi(x, y) \approx \sum_{p=1}^{P}\sum_{q=1}^{Q+1-p}\tilde{\psi}_{pq}\phi_{pq}(\xi_1, \xi_2) = \sum_{p=1}^{P}\sum_{q=1}^{Q+1-p}\tilde{\psi}_{pq}\varphi_p(\eta_1)\varphi_{pq}(\eta_2) \tag{24}$$

where (x, y), (ξ_1, ξ_2), and (η_1, η_2) are the coordinates of the physical domain, the standard triangular element, and the standard rectangular element respectively. Along the η_1 direction employed are the Gauss–Lobatto quadrature points and along the η_2 direction are the Gauss–Radau quadrature points in the present work. The basis functions chosen on the other hand are

$$\phi_{pq}(\xi_1, \xi_2) = \varphi_p(\eta_1)\varphi_{pq}(\eta_2) \tag{25}$$

$$\varphi_p(z) = \begin{cases}\dfrac{1-z}{2}, & p = 1 \\ \dfrac{1-z}{2}\dfrac{1+z}{2}P_{p-2}^{1,1}(z), & 1 < p < P \\ \dfrac{1+z}{2}, & p = P\end{cases} \tag{26}$$

and

$$\varphi_{pq}(z) = \begin{cases}\varphi_q(z), & p = 1 \text{ and } 1 \leq q \leq Q \\ \left(\dfrac{1-z}{2}\right)^p, & 1 < p < P \text{ and } q = 1 \\ \left(\dfrac{1-z}{2}\right)^p\dfrac{1+z}{2}P_{q-2}^{2p-1,1}(z), & 1 < p < P \text{ and } 1 < q < Q \\ \varphi_q(z), & p = P \text{ and } 1 \leq q \leq Q\end{cases} \tag{27}$$

where $P_n^{\alpha,\beta}$'s are the Jacobi polynomials of nth order having the orthogonality property of

$$\int_{-1}^{1}(1-x)^{\alpha}(1+x)^{\beta}P_n^{\alpha,\beta}(x)P_m^{\alpha,\beta}(x)dx = 0 \tag{28}$$

Finally, $P = Q$ is employed in this study.

3.3. Sub-cell approach

In this subsection, we describe how we take care of the discontinuities at the fluid–solid interface, that is Eqs. (9) and (23). Recall that the Gaussian quadrature integration is performed based on the Gauss–Lobatto quadrature points (η_{1i}) with weights w_{1i}'s along the η_1 direction and the Gauss–Radau quadrature points (η_{2j}) with weights w_{2j}'s along the η_2 direction, i.e.

$$\iint_{\Omega_4}f(\eta_1, \eta_2)d\eta_1 d\eta_2 = \sum_{i=1}^{P}\sum_{j=1}^{Q}f(\eta_{1i}, \eta_{2j})w_{1i}w_{2j} \tag{29}$$

where Ω_4 represents the standard rectangular element. The proposed sub-cell scheme starts from dividing the element into several sub-cells according to the weights as illustrated in Fig. 2. Each sub-cell
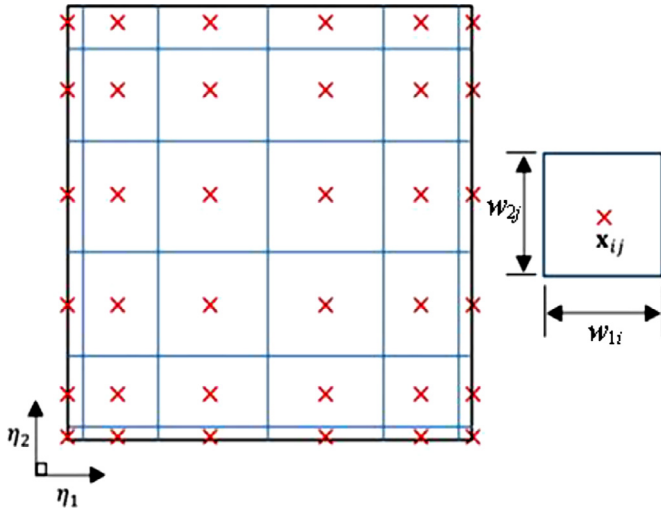
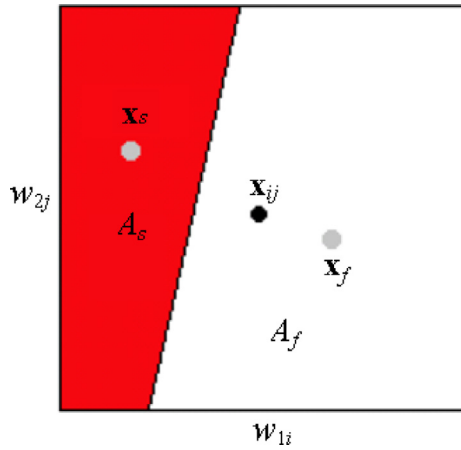**Fig. 2.** An illustration of sub-cells associated with a standard rectangular element as $P = Q = 6$.

Fig. 3. An example of a cut cell. The red part is solid and the remaining is fluid. (For interpretation of the references to colour in this figure legend, the reader is referred to the web version of this article).

therefore contains only one quadrature point ($\mathbf{x}_{ij}$) and has an area of $w_{1i} \times w_{2j}$.

These sub-cells can be distinguished into 3 types according to their overlapping condition with the solid body. The first (second) type of sub-cells called "solid (fluid) cells" is totally occupied by the solid body (fluid). Cells of the third type are partially occupied by solid and named "cut cells". For each cut-cell as illustrated in Fig. 3, we find the centroids ($\mathbf{x}_f$ and $\mathbf{x}_s$) and the areas (A_f and A_s) of the fluid and solid parts separately.

To smooth the density discontinuity, we define an area-weighted average density as follows

$$\rho = \begin{cases} \rho_s & \text{for quadrature points in the solid cells,} \\ (1-w_c)\rho_f + w_c\rho_s & \text{for quadrature points in the cut cells,} \\ \rho_f & \text{for quadrature points in the fluid cells.} \end{cases} \tag{30}$$

where

$$w_c = A_s/(w_i w_j) \tag{31}$$

The mass is conserved therefore. As far as the velocity is concerned, we choose the mass weighted averages instead in order to

conserve the linear momentum; consequently

$$\mathbf{u}^{n+1} = \begin{cases} \tilde{\mathbf{u}} & \text{for quadrature points in solid cells,} \\ \dfrac{w_c \rho_s \tilde{\mathbf{u}} + (1-w_c)\mathbf{u}^{***}\rho_f}{\rho} & \text{for quadrature points in cut cells,} \\ \mathbf{u}^{***} & \text{for quadrature points in fluid cells.} \end{cases} \tag{32}$$

Before we end this subsection, we would like to explain how the types of the sub-cells are identified and how the area fractions (w_c) are calculated. Before a simulation starts, an auxiliary Cartesian (square) mesh covering the whole computational domain is generated. A cell-link table [24] is built in advance, which stores the information of the Eulerian triangular elements overlapping with every 3 by 3 grid in the Cartesian mesh. At each time step, given the instantaneous location of a solid triangular element, we call out only the Eulerian elements in the cell-link table associated with the 3 by 3 grid in the middle square of which the centroid of the solid element is located. We judge which ones of them overlap with the solid element. If an Eulerian element does overlap with the solid element, we find out all the intersection points of the boundary lines of the solid element with the boundary lines of all sub-cells of the Eulerian element. Because the overlapped region of a sub-cell with the solid element is a polygon, the overlapped area and its centroid can be easily calculated based on the vertices of the polygon, which include the intersection points found above and possibly the vertices of the sub-cell and the vertices of the solid element. By accumulating contributions from all the solid elements, the solid area fractions of sub-cells of all Eulerian elements are obtained and so are the centroids of their fluid parts and solid parts.

Two things need special attention. One is that the above sorting algorithm is developed and performed preferably on the standard triangular element, because the mapping between a physical triangle and a standard triangle is linear and thus advantageous; it is easier however to explain the sub-cell concept on a standard rectangular element. The other one is that the grid size in the cell-link table must be large enough to ensure that every solid element can be accommodated within some 3 by 3 grid; it must thus be larger than the size of the solid elements therefore.

4. Numerical experiments

In this section, several numerical experiments were performed to verify the accuracy of the proposed solver. We first simulated a uniform flow past a fixed circular cylinder in Section 4.1. The sedimentation of a rigid circular cylinder in a rigid channel was simulated next in Section 4.2; a convergence test was finished to find out the order of accuracy of the proposed solver. Cylinders of other geometries were attempted eventually in Section 4.3.

4.1. Flow over a fixed circular cylinder

We consider a uniform flow past a fixed circular cylinder ($\mathbf{u}_s = 0$ cm/s) with $Re \equiv u_\infty D/\nu = 40$. The rigid circular cylinder has a density as the same as the fluid and a diameter of $D = 1$ cm. The computational domain is $[-10, 25] \times [-10, 10]$ cm^2) and the cylinder is fixed at the origin (0, 0) cm). The outflow boundary condition is employed at $x = 25$ cm and $\mathbf{u}_\infty = (u_\infty, v_\infty) = (1,0)$ cm/s) is imposed at the other three boundaries. For comparison, we also solved the same flow by using the spectral element solver with a body-fitted mesh. Fig. 4 shows the Eulerian meshes in the neighborhood of the cylinder and Fig. 5 shows the Lagrangian mesh for the circular cylinder. Other numerical parameters employed are the expansion order $P = 9$, the time step $\Delta t = 0.001$ s), and the penalization factor $\lambda \Delta t = 10^6$.

The pressure contours from both schemes are shown in Fig. 6. An excellent agreement is observed. Next we compare the length of the
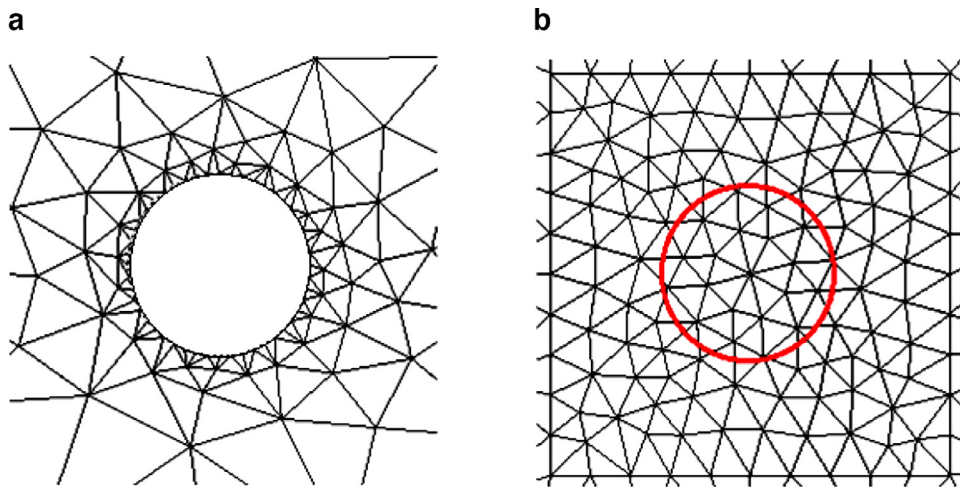
a **b**

Fig. 4. The body-fitted mesh (a) and non-body-fitted (immersed-boundary) mesh, (b) employed in the neighborhood of the circular cylinder.
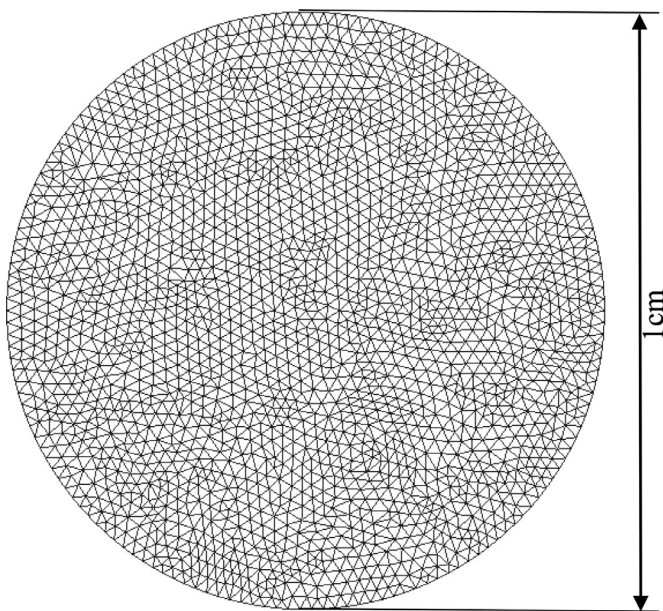

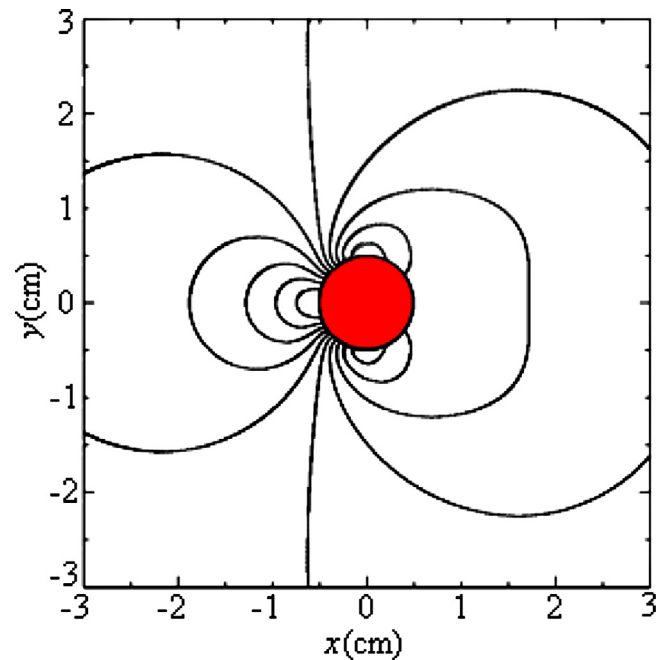**Fig. 5.** The Lagrangian mesh employed for the circular cylinder.

Fig. 6. Pressure contours at Re = 40 obtained based on the immersed-boundary mesh (solid lines) and based on the body-fitted mesh (dotted lines).

Table 1
Comparison of the length of the trailing bubble and the separation angle at Re = 40.

Re = 40	L/D	θ_s (degree)
Present result		
body-fitted-mesh	2.25	53.9°
Immersed-boundary mesh	2.24, 2.24 [19]	53.8°, 53.8° [19]
Calhoun [25]	2.18	54.2°
Russell and Wang [26]	2.29	53.1°
Fornberg [27]	2.24	—
Dennis and Chang [28]	2.35	53.8°

Table 2
Strouhal numbers at Re = 100 and 200.

	Re = 100	Re = 200
Present results		
Body-fitted-mesh	0.170	0.201
Immersed-boundary mesh	0.170, 0.170 [19]	0.200, 0.200 [19]
Calhoun [25]	0.175	0.202
Russell and Wang [26]	0.169	0.195
Liu, Zheng [29]	0.165	0.192
Roshko [30]∗	0.167	0.190
Williamson [31]∗	0.164	0.197

∗ interpolated from experimental measurements

trailing bubble (L) and the separation angle (θ_s) with data in literature as shown in Table 1, including those obtained by the previous version of the present solver [19]. The results are all very close.

Flows with Re = 100 and 200 were also simulated. In Table 2 we show the obtained Strouhal numbers together with data in literature. Agreement is once again obtained.

4.2. Freely falling circular cylinder

To test the order of the accuracy of the proposed solver, especially for two-way coupling problems, we simulated the freely falling motion of a rigid circular cylinder in a channel of width W = 4 cm;
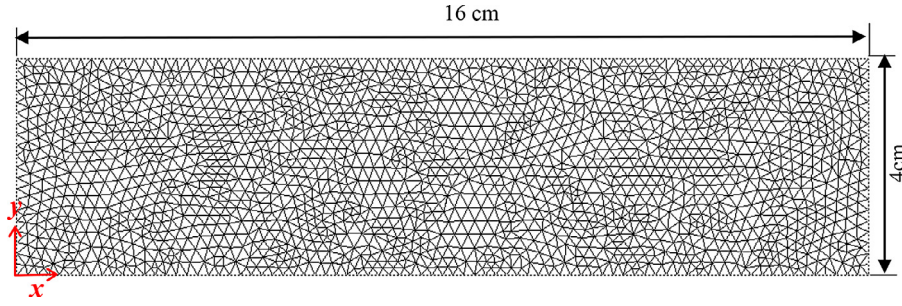
Fig. 7. The Eulerian mesh employed for the simulation of the sedimentation of a circular cylinder.

the computational domain prepared is $[0, 16] \times [0, 4]$ cm^2. Herein we choose $\rho_f = 1$ g/cm^3 and $\nu = 10$ cm^2/s. The circular cylinder, initially located at the position $(6, 2)$ cm, has a diameter of $D = 1$ cm and is free to fall from rest under the gravity of $\mathbf{g} = (981, 0)$ cm/s^2. Three solid densities: $\rho_s = 1.05$, 1.1, and 1.15 g/cm^3 were attempted. Fig. 7 shows the Eulerian mesh for this simulation. It has a total of 3394 triangular elements which average side size (ΔL_f) is $0.2D$. The Lagrangian mesh for tracing the cylinder is the same as the one shown in Fig. 5; the averaged side size of the Lagrangian elements (ΔL_s) is $0.04D$, about 1/5 of the Eulerian mesh. Furthermore, 9×9 Gaussian quadrature points were employed for the solid-area integration. According to the suggestion of Zhang and Gay [32], the resolution of the Lagrangian mesh should be at least twice as high as that of the Eulerian mesh. Herein, we chose an even higher resolution for the sake of capturing the solid shape more precisely and for the sake of keeping the numerical errors arising from the solid-area integration minor. The zero velocity boundary condition is imposed on all the four walls of the channel. The time step is $\Delta t = 5 \times 10^{-5}$ s) and the penalization factor employed is $\lambda \Delta t = 10^6$.

Because the solid-fluid density ratio of interest is small, the Reynolds number based on the terminal velocity, $Re = V_t D/\nu$, is expected to be very small too. Therefore the analytical solution from Happel and Brenner [33] is applicable:

$$V_t = \frac{(\rho_s/\rho_f - 1)D^2 g}{16\nu}$$
$$\times \left[\ln\left(\frac{W}{D}\right) - 0.9157 + 1.7244\left(\frac{D}{W}\right)^2 - 1.7302\left(\frac{D}{W}\right)^4 \right]$$

(33)

In Fig. 8, we show the evolutions of the x-velocity component (u_T) of the mass center of the cylinder superimposed with the analytical terminal velocities. The simulated and the analytical terminal velocities match pretty well. The relative errors are all below 2%.

We now focus on the case of $\rho_s = 1.1$ g/cm^3 and perform a convergence test by varying the expansion order P. For each simulation, we take the average value during the time period t = 0.2∼0.4 s) as the simulated terminal velocity $\bar{V}$. Fig. 9 shows that the simulated terminal velocity increases and converges gradually with the increasing expansion order P. By taking the value obtained when $P = 17$ ($\bar{V}_{P=17}$) as the exact value, we plot the error $e_v \equiv |\bar{V} - \bar{V}_{P=17}|$ against the expansion order P in Fig. 10. As seen, the order of accuracy is between 2 and 3. Although a spectral accuracy is expected for spectral methods, the use of the immersed boundary skill and the local smoothing near the solid–fluid interface must cause a reduction of the accuracy. In fact, the proposed "sub-cell scheme" is more like a 2nd order interpolation scheme; so is the piecewise linear approximation of the solid shape. Furthermore, the terminal velocity is a result of a balance between the gravity force and the total drag; the influence of local errors must be less significant and therefore an order of accuracy slightly greater than 2 is observed.
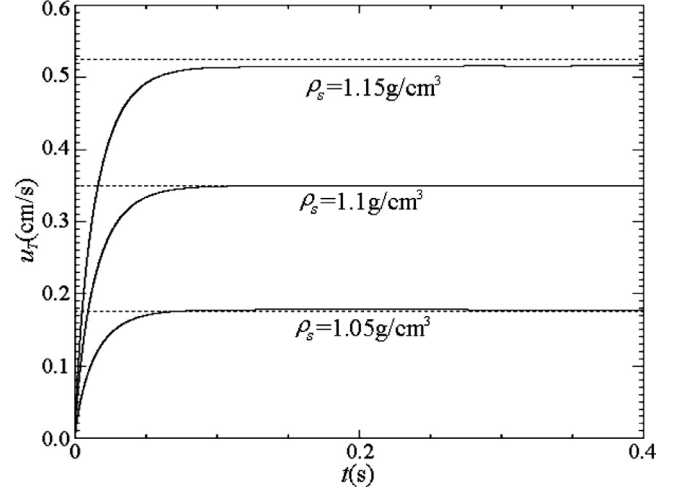

Fig. 8. The evolution of the x component of the translational velocity (u_T) of the cylinder as $P = 17$ (solid lines), superimposed with the analytical terminal velocities (dotted lines).
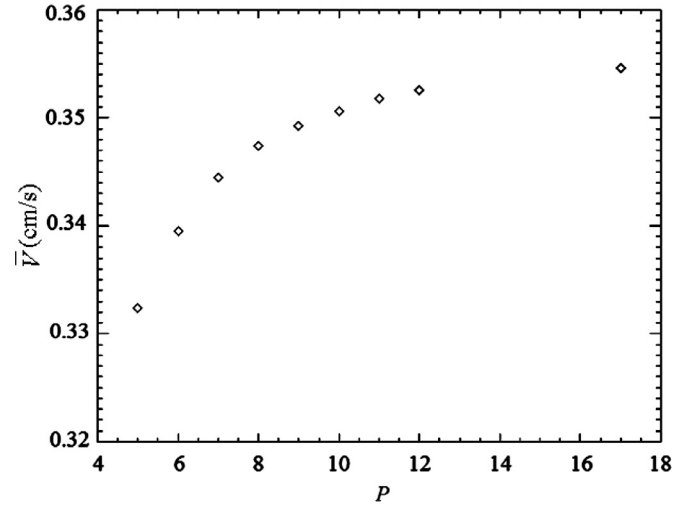

Fig. 9. The convergence of the simulated terminal velocity against the expansion order P.

To further explore the accuracy of the proposed solver, we also examine the detailed flow field near the fluid–solid interface. We target at the pressure distribution on the surface of the cylinder, namely $p(\theta)$ for $0 \leq \theta \leq 2\pi$. The maximum absolute difference, $e_p \equiv \max_{0 \leq \theta \leq 2\pi} |p - p_{P=17}|$, is measured and presented in Fig. 11. An accuracy of order 2 is observed. Figs. 10 and 11 indicate that a local physical variable converges slower than a global one which is not out of expectation for an immersed-boundary-type scheme.
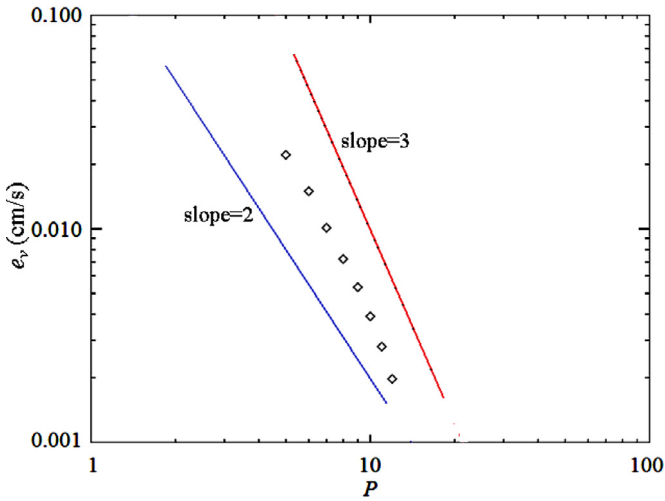
Fig. 10. The error associated with the terminal velocity against the expansion order P.
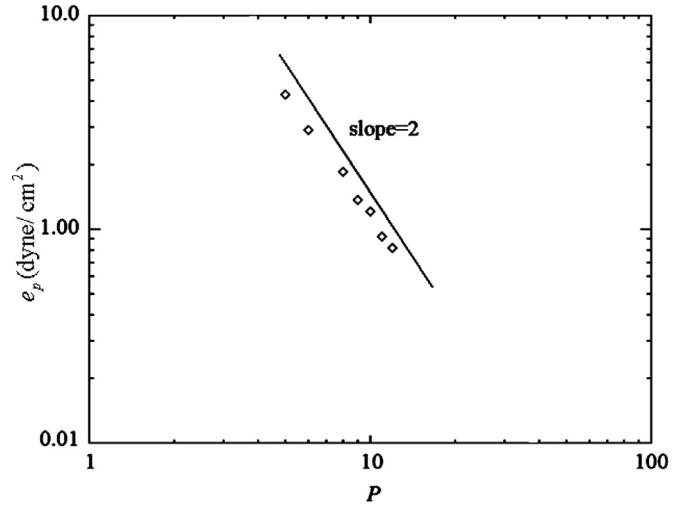

Fig. 11. The maximum error in the pressure around the cylinder against the expansion order P.

4.3. Freely falling cylinders of other geometrics

To test the geometric capability of the proposed solver, we test square, regular triangular, and elliptic cylinders in this subsection. The Lagrangian meshes employed are shown in the Fig. 12.

The square and triangular cylinders are falling in a channel with a dimension of $[0, 40] \times [0, 4]$ cm^2. Both have a cross sectional area as large as that of a circular cylinder of diameter $D = 1$ cm. Like what Wachs did [34], the mass centers of the cylinders are initially located at $(6, 1.95)$ cm, slightly offset from the centerline in order to inspire possible oscillating motion. The fluid has a density of $\rho_f = 1$ g/cm^3 and a viscosity of $\nu = 0.08$ cm^2/s; two solid densities are tested: $\rho_s = 1.0002$ and 1.01 g/cm^3. The average side sizes of the Eulerian and Lagrangian elements are $\Delta L_f = 0.2D$ and $\Delta L_s = 0.04D$, respectively. Other numerical parameters employed are the expansion or-

Table 3
The terminal velocities of the freely falling square and triangular cylinders.

Cross section		Square		Regular triangle
Density (g/cm^3)		1.0002	1.01	1.0002
Terminal velocity (cm/s)	Present	8.22×10^{-2}	2.12	6.96×10^{-2}
	Wachs [34]	8.00×10^{-2}	2.10	6.64×10^{-2}

der $P = 9$, the time step $\Delta t = 0.005$ s, and the penalization factor $\lambda \Delta t = 10^6$. The resulting terminal velocities of the square and triangular cylinders are shown in Table 3. The present results are very close to those obtained by Wachs [34].

The elliptic cylinder is falling in a channel of $[0,12] \times [0,2]$ cm^2 instead. Initially it is located at $(1,1)$ cm with three different orientations: $5°$, $45°$, and $90°$ as shown in Fig. 13. The ellipse has a semi-major
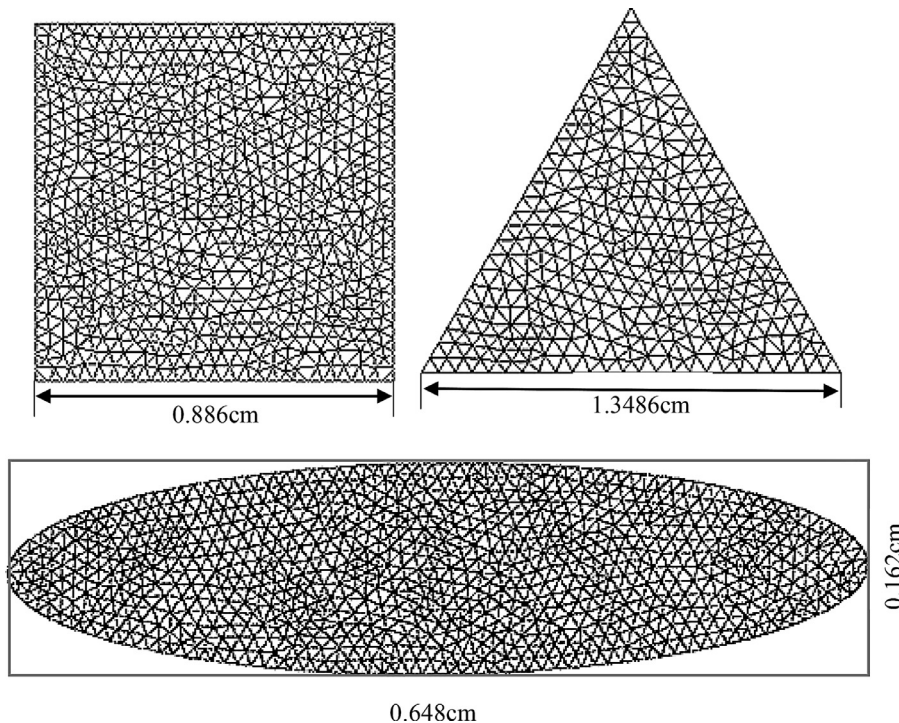

Fig. 12. The Lagrangian meshes for the square, triangular, and elliptic cylinders.
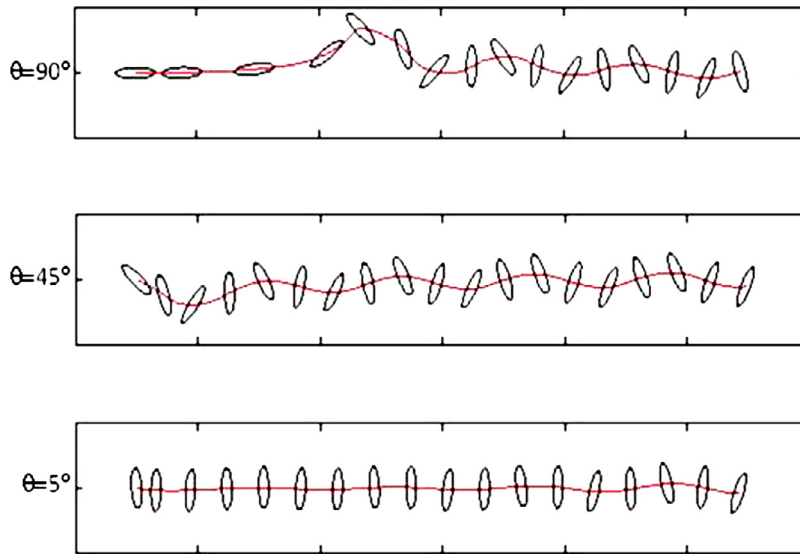
Fig. 13. The instantaneous locations and orientations of the ellipse at several different times and the trajectories of its mass center (red curves). (For interpretation of the references to colour in this figure legend, the reader is referred to the web version of this article).
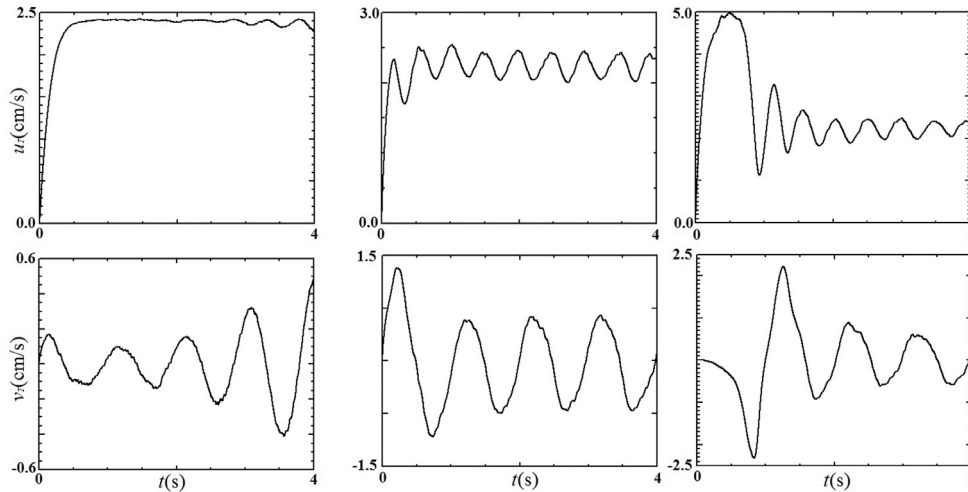

Fig. 14. The evolutions of the velocity components (u_T, v_T) of an ellipse with an initial orientation of $\theta = 5°$, $45°$, and $90°$ (from left to right).

axis of $a = 0.324$ cm, a semi-minor axis of $b = 0.081$ cm, and a density of $\rho_s = 1.25$ g/cm³. The fluid has a density of $\rho_f = 1$ g/cm³ and a viscosity of $\nu = 0.1$ cm²/s. The averaged side sizes of the Eulerian and the Lagrangian elements are chosen to be 0.1 cm and 0.02 cm, respectively. Other numerical parameters employed are the expansion order $P = 9$, the time step $\Delta t = 0.0005$ s, and the penalization factor $\lambda \Delta t = 10^6$.

Fig. 13 shows the instantaneous locations and orientations of the ellipse at several different times; the red curves are the trajectories of its mass center. As seen, with an initial orientation of $\theta = 45°$, the ellipse starts fluttering as soon as it is released. This phenomenon was also observed by Finn [35]. When the initial orientation is $\theta = 90°$, the ellipse goes straight down during the early time period but deviates away from the centerline of the channel later and eventually flutters like the previous case. The motion of the ellipse is the most stable one when it is having an initial orientation of $\theta = 5°$; it keeps on falling straight down until the very end of the simulation. According to the evolution of velocity components, (u_T, v_T), of the mass center as shown in Fig. 14, periodic fluttering motion might be expected in all cases if the channel is sufficiently long; the

final behavior of the cylinder is seemingly independent of the initial orientation.

5. Conclusion

A 2D simulation method was developed to solve the two-way coupling problems between an incompressible viscous fluid and a rigid body. It is developed based on the spectral element method and the immersed boundary concept. The whole system is modeled as a non-uniform density flow and the rigid body motion is enforced by the penalization method. A Lagrangian mesh is employed to trace the rigid body and a so-called sub-cell approach is constructed to deal with the discontinuity at the solid–fluid interface. The proposed scheme was found to be 2nd-order accurate and its geometric flexibility was confirmed. With this geometric flexibility arising from the use of the spectral element method as well as the use of a Lagrangian mesh, the present scheme is applicable to flow induced by rigid bodies of arbitrary shapes in channels with complicated wall boundaries. Numerical instabilities associated with high density-ratio and high Reynolds-number flow need further improving however.

Acknowledgment

References

[1] Peskin CS, Mcqueen DM. Modeling prosthetic heart-valves for numerical-analysis of blood-flow in the heart. J Comput Phys 1980;37:113–32.

[2] Peskin CS, Mcqueen DM. A 3-dimensional computational method for blood-flow in the Heart .1. Immersed elastic fibers in a viscous incompressible fluid. J Comput Phys 1989;81:372–405.

[3] Peskin CS, Printz BF. Improved volume conservation in the computation of flows with immersed elastic boundaries. J Comput Phys 1993;105:33–46.

[4] Mohd-Yusof J. Combined immersed boundary/B-spline methods for simulations of flow in complex geometries. In: Annual Research Briefs, Center for Turbulence Research; 1999. p. 317–27.

[5] Glowinski R, Pan TW, Hesla TI, Joseph DD, Periaux J. A fictitious domain approach to the direct numerical simulation of incompressible viscous flow past moving rigid bodies: application to particulate flow. J Comput Phys 2001;169:363–426.

[6] Yu ZS, Shao XM. A direct-forcing fictitious domain method for particulate flows. J Comput Phys 2007;227:292–314.

[7] Gallier S, Lemaire E, Lobry L, Peters F. A fictitious domain approach for the simulation of dense suspensions. J Comput Phys 2014;256:367–87.

[8] Sharma N, Patankar NA. A fast computation technique for the direct numerical simulation of rigid particulate flows. J Comput Phys 2005;205:439–57.

[9] Apte SV, Martin M, Patankar NA. A numerical method for fully resolved simulation (FRS) of rigid particle-flow interactions in complex flows. J Comput Phys 2009;228:2712–38.

[10] Apte SV, Finn JR. A variable-density fictitious domain method for particulate flows with broad range of particle-fluid density ratios. J Comput Phys 2013;243:109–29.

[11] Coquerelle M, Cottet GH. A vortex level set method for the two-way coupling of an incompressible fluid with colliding rigid bodies. J Comput Phys 2008;227:9121–37.

[12] Gazzola M, Chatelain P, van Rees WM, Koumoutsakos P. Simulations of single and multiple swimmers with non-divergence free deforming geometries. J Comput Phys 2011;230:7093–114.

[13] Zhang L, Gerstenberger A, Wang XD, Liu WK. Immersed finite element method. Comput Meth Appl Mech Eng 2004;193:2051–67.

[14] Lee TR, Chang YS, Choi JB, Kim DW, Liu WK, Kim YJ. Immersed finite element method for rigid body motions in the incompressible Navier–Stokes flow. Comput Meth Appl Mech Eng 2008;197:2305–16.

[15] Wang XS, Wang C, Zhang LT. Semi-implicit formulation of the immersed finite element method. Comput Mech 2012;49:421–30.

[16] Parussini L, Pediroda V. Fictitious domain approach with hp-finite element approximation for incompressible fluid flow. J Comput Phys 2009;228:3891–910.

[17] Warburton TC, Sherwin SJ, Karniadakis GE. Basis functions for triangular and quadrilateral high-order elements. Siam J Sci Comput 1999;20:1671–95.

[18] Karniadakis GE, Sherwin SJ. Spectral/hp element methods for CFD, Numerical Mathematics and Scientific Computation. Oxford University Press; 1999.

[19] Chen L-C, Huang M-J. A spectral-element simulator for two-dimensional rigid-body-fluid interaction problems. In: Iványi P, Topping BHV, editors. Proceedings of the Ninth International Conference on Engineering Computational Technology, Civil-Comp Press, Stirlingshire, UK; 2014 Paper 77.

[20] Angot P, Bruneau CH, Fabrie P. A penalization method to take into account obstacles in incompressible viscous flows. Numerische Mathematik 1999;81:497–520.

[21] Bost C, Cottet GH, Maitre E. Convergence analysis of a penalization method for the three-dimensional motion of a rigid body in an incompressible viscous fluid. Siam J Numer Anal 2010;48:1313–37.

[22] Gear CW. Numerical initial value problems in ordinary differential equations, xvii. Englewood Cliffs, N.J.: Prentice-Hall; 1971. Prentice-Hall series in automatic computation p. 253.

[23] Karniadakis GE, Israeli M, Orszag SA. High-order splitting methods for the incompressible navier stokes equations. J Comput Phys 1991;97:414–43.

[24] Verlet L. Computer experiments on classical fluids .I. thermodynamical properties of lennard-jones molecules. Phys Rev 1967;159 98-&.

[25] Calhoun D. A Cartesian grid method for solving the two-dimensional streamfunction-vorticity equations in irregular regions. J Comput Phys 2002;176:231–75.

[26] Russell D, Wang ZJ. A cartesian grid method for modeling multiple moving objects in 2D incompressible viscous flow. J Comput Phys 2003;191:177–205.

[27] Fornberg B. A numerical study of steady viscous-flow past a circular-cylinder. J Fluid Mech 1980;98:819–55.

[28] Dennis SCR, Chang GZ. Numerical solutions for steady flow past a circular cylinder at reynolds numbers up to 100. J Fluid Mech 1970;42 471-&.

[29] Liu C, Zheng X, Sung CH. Preconditioned multigrid methods for unsteady incompressible flows. J Comput Phys 1998;139:35–57.

[30] Roshko A. On the development of turbulent wakes from vortex streets. NACA Rep 1954;1191.

[31] Williamson CHK. Defining a universal and continuous Strouhal–Reynolds number relationship for the laminar vortex shedding of a circular-cylinder. Phys Fluids 1988;31:2742–4.

[32] Zhang LT, Gay M. Immersed finite element method for fluid-structure interactions. J Fluids Struct 2007;23:839–57.

[33] Happel J, Brenner H. Low Reynolds number hydrodynamics: with special applications to particulate media. Prentice-Hall; 1965.

[34] Wachs A. A DEM-DLM/FD method for direct numerical simulation of particulate flows: sedimentation of polygonal isometric particles in a Newtonian fluid with collisions. Comput Fluids 2009;38:1608–28.

[35] Finn DL. Falling paper and flying business cards. SIAM News 2007;40:1–3.